Effect of Complex Inclusion Particles on the Solidification Structure of Fe-Ni-Mn-Mo Alloy

JUN SEOK PARK, CHANGHEE LEE, and JOO HYUN PARK

The effect of combinations of several deoxidizers, *i.e.*, Mg-Al, Mg-Ti, Al-Ti, and Ce-Al, on the solidification structure of Fe-2 mass pct Ni-1 mass pct Mn-1 mass pct Mo alloy melt was investigated using a melt sampling and quenching method. Using this method, we evaluated the catalytic potency of several complex inclusion particles by taking the inclusion evolution process into account. Fine equiaxed crystals were obtained in the Mg-Ti-deoxidized steel wherein the $MgO(MgAl_2O_4)$-TiN complex compounds formed. However, the longer the holding time at high temperatures, the larger the fraction of Ti_2O_3, and very fine TiN formed because of microsegregation during solidification, resulting in poor equiaxed crystals. When the steel was deoxidized with Mg-Al, the initial structure was dominantly columnar. However, the longer the holding time, the larger the fraction of $MgAl_2O_4$ spinel, resulting in the formation of fine equiaxed crystals. Ce-Al complex deoxidation provided a relatively small portion of equiaxed crystals, whereas Ti-Al deoxidation produced the fewest equiaxed crystals because of the formation of alumina. The effectiveness of each inoculant particle for the crystallization of the primary δ-iron was explained well by the lattice disregistry concept.

DOI: 10.1007/s11663-012-9734-3

I. INTRODUCTION

GRAIN refinement has been investigated as an approach to improve the mechanical properties of steel welds.[1] Several research groups have attempted to refine the grain size of the heat-affected zone (HAZ) by enhancing the nucleation of acicular ferrite on the surfaces of oxide and sulfide inclusions.[2–17] Grong and Matlock reported that microstructures consisting of acicular ferrite provided weld metal and the HAZ with good mechanical properties such as strength and toughness.[2] Grong *et al.*[1,2,14] found that the volume fraction of acicular ferrite was strongly dependent on the chemistry of oxide particles, which was affected mainly by the [Al]/[O] ratio. Koseki and Thewlis also reported that the acicular ferrite volume fraction increased markedly at a [Al]/[O] ratio of around 1.0 in gas-shielded metal arc welds, corresponding to the presence of the $MnAl_2O_4$ (galaxite) spinel.[7] Terasaki and Komizo directly observed the acicular ferrite grown from the inclusion surface using laser scanning confocal microscopy (LSCM).[15]

Ito and Nakanishi[18] and Mori *et al.*[19] found that TiO and TiN phases in the inclusion surface layers significantly increased the acicular ferrite volume fraction.[7] Yamada *et al.*[16] also observed that a Ti-enriched layer existed at the interface between the amorphous phase and $MnAl_2O_4$ oxide in low carbon submerged arc weld metal and considered that a Ti-enriched layer of a Ti-O system contributed to the decrease in interfacial energy between inclusions and ferrite. Later, Nishizawa proposed that TiO could facilitate grain refinement based on its metallic bond character.[20] Koseki and Thewlis stated that in low Al-content weld metals, oxygen is available for Ti-oxide formation, whereas when the Al content is high, oxygen is killed by Al and little is left for Ti-oxide formation.[7] They concluded that the most effective nucleants for acicular ferrite in weld metals are the crystalline phases of TiO and TiN, and the galaxite spinel $MnAl_2O_4$.[7]

Several experimental and model-based studies have been performed to understand the fundamental phenomena underlying the heterogeneous nucleation of delta ferrite in various kinds of substrate particles during solidification processes. Bramfitt investigated the effects of various carbides and nitrides on the critical undercooling of the iron melt and proposed that lattice disregistry was an important factor affecting the efficiency of heterogeneous nucleation.[21] Similar results were obtained for several oxide inclusions by Ohashi *et al.*[22] Recently, Nakajima *et al.*[23] measured the critical undercooling of iron alloys using differential scanning calorimetry (DSC) and found that the undercooling values previously measured by different authors showed a wide scatter, which originated from different experimental methods in each study. However, these authors confirmed that critical undercooling was small in the order of TiN, Al_2O_3, and Ti_2O_3, and that the catalytic potency of TiN was the greatest.[23] This was qualitatively explained by Bramfitt's relation.

JUN SEOK PARK, Graduate Student, and JOO HYUN PARK, Professor, are with the School of Materials Science and Engineering, University of Ulsan, Ulsan 680-749, South Korea. Contact e-mail: basicity@mail.ulsan.ac.kr CHANGHEE LEE, Professor, is with the Department of Material Science and Engineering, Hanyang University, Seoul 133-791, South Korea.

Manuscript submitted: December 1, 2011.
Article published online September 28, 2012.

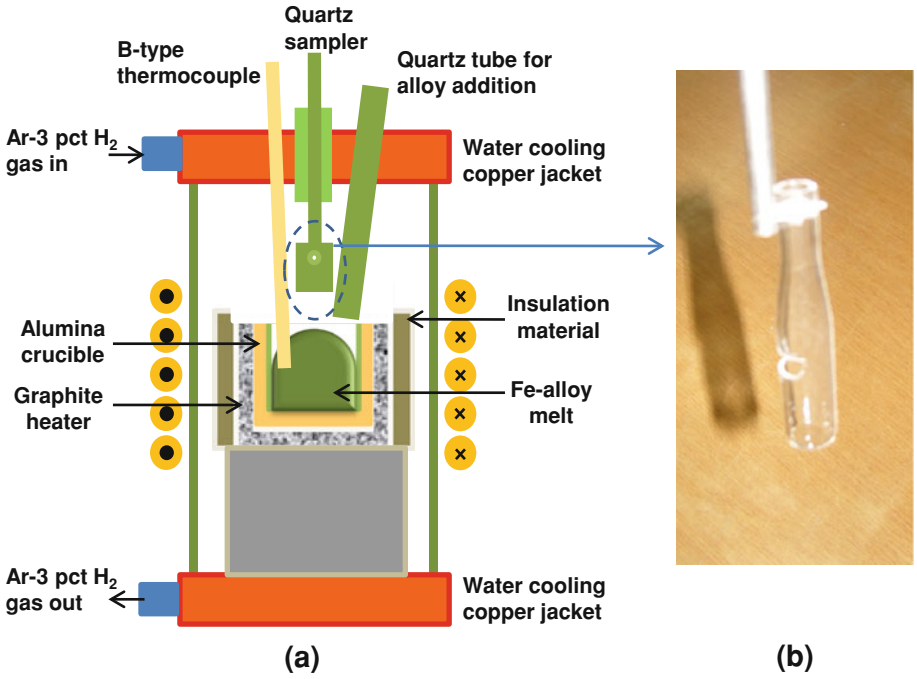

Fig. 1—Schematic diagram of the experimental apparatus (*a*) and quartz sampler used in this study (*b*).

In a later study, Nakajima *et al.*[24] reported that critical undercooling of the Fe-10 mass pct Ni alloy melt increased as the number of smaller particles decreased and the number of larger particles increased. Furthermore, they reported that for the same amount of deoxidizer, the undercooling for primary crystals of the γ-iron occurred in the order of MgO, ZrO_2, Al_2O_3, and then $CaO\text{-}Al_2O_3$. However, these authors did not explain these findings. The effect of inclusion density on the solidification structure of iron alloys was systematically investigated by Suito *et al.*[25–28] Recently, we investigated the formation of TiN single particles as well as $MgAl_2O_4$-TiN complex particles in Ti-containing ferritic (11 mass pct Cr) stainless steel and found that inclusion of these particles resulted in a fine equiaxed structure because of low disregistry not only between TiN and delta ferrite, but also between TiN and $MgAl_2O_4$ spinel.[29] A bimodal distribution of the above non-metallic compounds was critically important to refine the solidification structure. Koseki *et al.*,[30] based on Monte Carlo simulations, reported that the columnar-to-equiaxed transition (CET) can be promoted both by increasing the density of TiN and the content of soluble Ti in the gas tungsten arc welding of 17 mass pct Cr stainless steel.

In the current study, we therefore investigated the effects of combinations of several deoxidizers, *i.e.*, Mg-Al, Mg-Ti, Al-Ti, and Ce-Al, on the solidification structure of Fe-Ni-Mn-Mo alloy melt using a melt sampling and quenching methodology. By employing this method, which we chose to simulate the very fast cooling conditions during welding, we were able to evaluate the catalytic potency of several complex inclusion particles by taking the inclusion evolution process into account.

II. EXPERIMENTAL

A Fe-2 mass pct Ni-1 mass pct Mn-1 mass pct Mo (600 g) alloy was melted at 1873 K (1600 °C) in a fused alumina crucible (60 mm OD × 52 mm ID × 120 mm HT) with a graphite heater under a purified Ar-3 vol pct H_2 gas atmosphere using an induction furnace, as shown in Figure 1. Alloy samples were prepared by mixing electrolytic iron (3N purity) and manganese (3N), and high purity nickel (4N) and molybdenum (4N). Temperature was controlled by a B-type thermocouple covered by an alumina sheath. After the temperature reached 1873 K (1600 °C), various kinds of deoxidizers, *i.e.*, 0.2 mass pct Mg-0.2 mass pct Al, 0.2 mass pct Ce-0.2 mass pct Al, 0.2 mass pct Mg-0.2 mass pct Ti, or 0.2 mass pct Ti-0.2 mass pct Al, were added into the melt under an inert atmosphere. Each inoculant-containing alloy was prepared in advance as Ni-20 mass pct Ce, Ni-16 mass pct Mg, and Ni-35 mass pct Ti alloys using a vacuum arc melter.

The steel samples were passed through a quartz sampler 5, 15, 30, and 60 minutes after deoxidizer addition. To estimate the heterogeneous nucleation tendency during rapid solidification, each sample was directly quenched by dipping it into brine within 5 seconds of sampling. Each sample was cut vertically for chemical analysis and to observe the solidification structure. The solidification structures were revealed by etching in Oberhöffer solution (1 g cupric chloride, 30 g ferric chloride, 0.5 g stannous chloride, 50 ml HCl, 500 ml distilled water, and 500 ml ethyl alcohol).[31] The chemical composition of each sample was determined by inductively coupled plasma atomic emission spectrometry (ICP-AES, IRIS Advantage (REG), Thermo Electron, Waltham, MA), and the nitrogen and oxygen

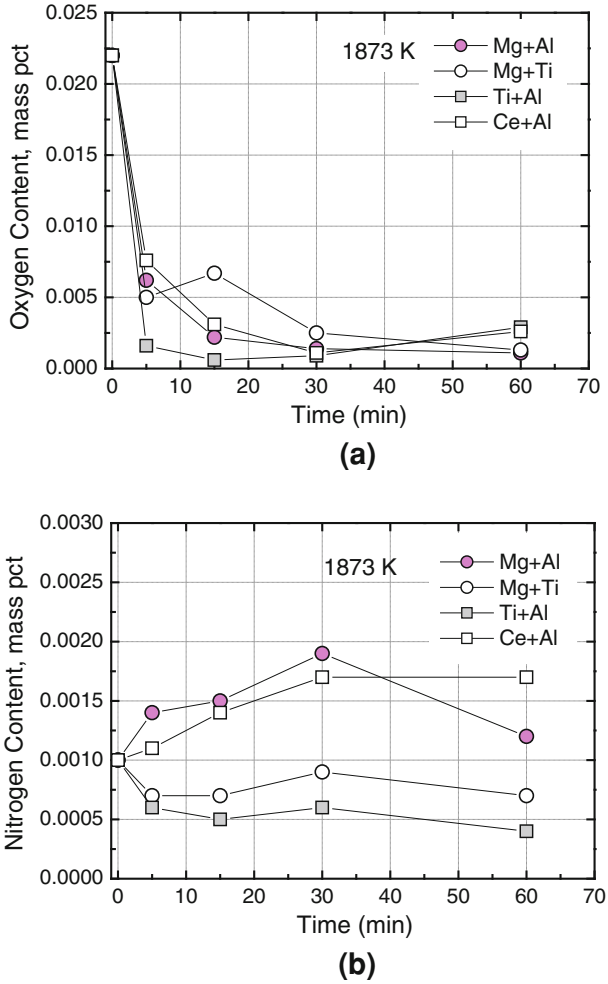

Fig. 2—Changes in total oxygen content (*a*) and total nitrogen content (*b*) in melt with time.

contents of the samples were analyzed using a combustion analyzer.

To characterize the inclusions in the steel samples, a metal sample (from 0.2 to 0.3 g) was dissolved in 10 pct AA (10 pct acetylacetone—1 pct tetramethylammonium chloride—methanol) solution using a potentiostatic electrolytic extraction method under a total electric charge ranging from 4000 to 5000 coulombs (500 mA current, from 2 to 3 hours).[32] To prepare 10 pct AA solution, tetramethylammonium chloride (10 g) was dissolved in acetylacetone solution (100 ml), followed by the addition of methanol to a total volume of 1 L. The electrolyte solution was vacuum-filtered using a membrane filter with an open pore size of 0.2 μm. The number and size distributions, three-dimensional morphology, and chemical compositions of the residual particles on the filter were analyzed using a scanning electron microscope equipped with an energy dispersive spectroscope (SEM-EDS, JSM-840A, JEOL) with a link detector and an automatic image analysis system. The chemistry of the inclusion particles could be quantitatively analyzed because excitation from the steel matrix was excluded using this methodology. The number (from 300 to 400 particles per sample) and size of the inclusions were analyzed statistically by observing 3000× images of each sample. We obtained the equivalent circular diameter, referred to as the "Heywood diameter," using this approach.

III. RESULTS

After the deoxidizers were added to the alloy melts, the total oxygen content decreased with increasing reaction time, as shown in Figure 2, indicating the continuous formation of oxide inclusions. When Ti was added, the total nitrogen content in the melt decreased slightly, probably because of the formation of TiN. The changes in the concentrations of each deoxidizer are shown in Figure 3. When the combinations of Mg-Al, Mg-Ti, and Ce-Al were added for deoxidation, the content of Mg and Ce decreased continuously with increasing time, whereas levels of Al and Ti remained stable throughout the experiments. These observations can be explained by the fact that the vapor pressure of magnesium is high and the affinity between Ce and O is greater than that between Al and O. The latter is confirmed by the difference in the Gibbs free energy of the formation of Al_2O_3 and Ce_2O_3 as follows:[33]

$$2[\mathrm{Al}] + 3[\mathrm{O}] = \mathrm{Al_2O_3(s)}, \quad \Delta G^\circ = -450.7\,\mathrm{kJ/mol\ at\ 1873\,K (1600\,^\circ C)} \qquad [1]$$

$$2[\mathrm{Ce}] + 3[\mathrm{O}] = \mathrm{Ce_2O_3(s)}, \quad \Delta G^\circ = -604.5\,\mathrm{kJ/mol\ at\ 1873\,K\ (1600\,^\circ C)} \qquad [2]$$

In the case of Al-Ti deoxidation, the Ti yield was slightly higher than that of Al because of the greater affinity between Al and O than that between Ti and O.

The solidification structures of the 30- and 60-minute samples are shown in Figure 4. Mg-Ti deoxidation resulted in the formation of fine equiaxed crystals throughout the 30-minute sample. In cases of Ce-Al and Mg-Al complex deoxidation, partially equiaxed crystals were observed, whereas very poor equiaxed crystals formed in samples subjected to Ti-Al deoxidation. However, a different structural tendency was noted in the 60-minute samples compared to the 30-minute samples. In samples to which Mg-Ti was added, no equiaxed crystals were observed, while the fraction of equiaxed crystals in the samples deoxidized with the increased amount of Mg-Al. The reasons for the above experimental findings can be understood by the characteristics of the inclusions and the number density, which are summarized in Table I.

IV. DISCUSSION

A. *Evolution of Non-Metallic Inclusions*

1. *Mg-Al deoxidation*

After Mg and Al were added to the melt as catalyst-forming elements, the single and complex oxides of

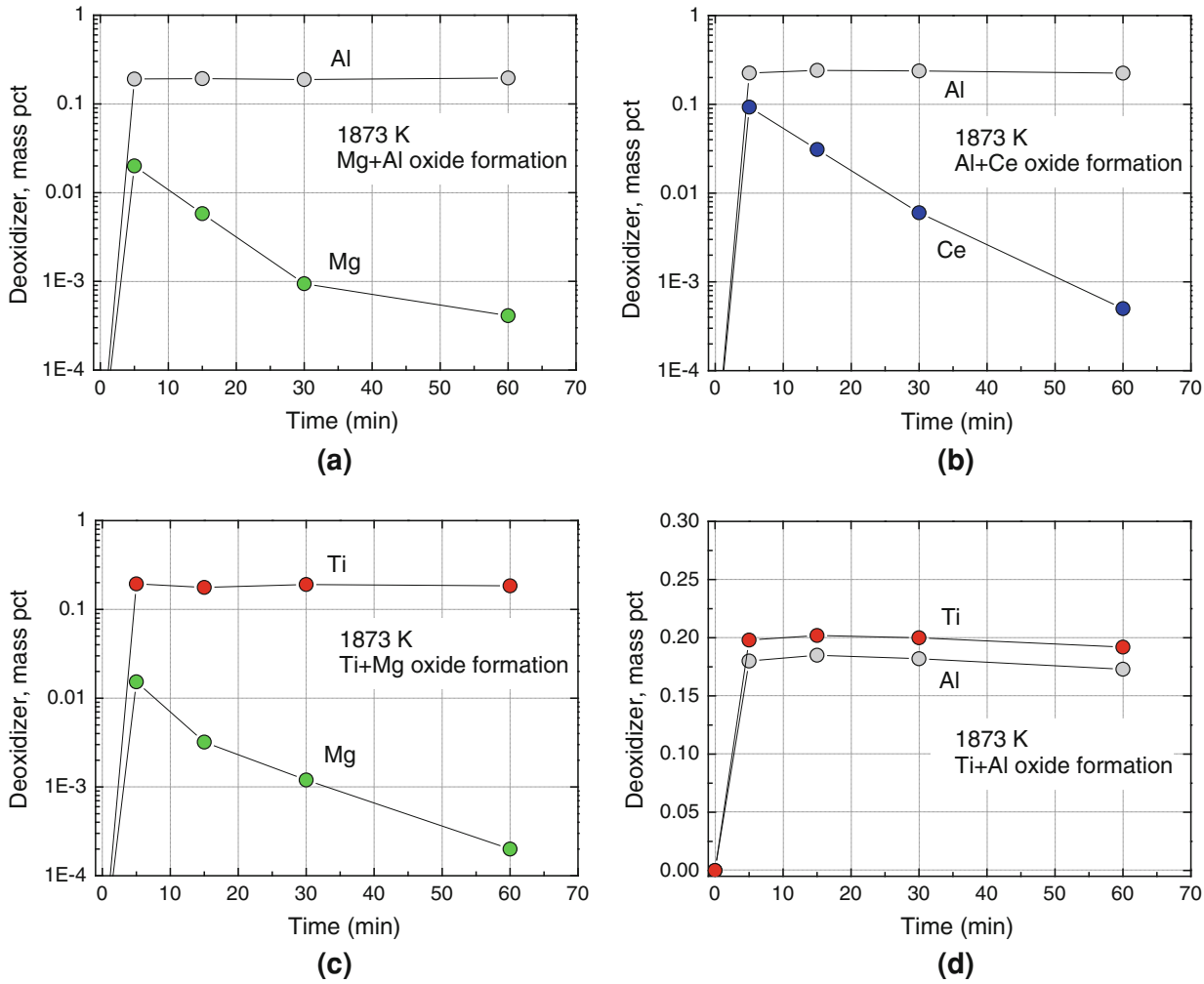

Fig. 3—Changes in the content of deoxidizer in the case of Mg-Al (*a*), Ti-Al (*b*), Mg-Ti (*c*) and Ce-Al (*d*) complex deoxidation at 1873 K (1600 °C).

Al_2O_3 and $MgAl_2O_4$ (spinel) formed. However, as shown in Figure 5, the dominant inclusion phase changed from alumina in the 30-minute sample to spinel in the 60-minute sample. The alumina initially had a spherical shape because of large supersaturation followed by agglomeration because of poor wettability to molten steel. Based on a previous review on the formation mechanisms of spinel inclusions in molten steel,[34] a certain amount of incubation time is required for the formation of spinel inclusions, consistent with our results. The number density of inclusions decreased with increasing time, as shown in Table I. As shown in Figure 5, alumina agglomerates were not observed in the 60-minute sample but small spherical alumina particles were still present, presumably because large alumina agglomerates can easily float upward to the melt surface based on the following equation derived from Stoke's law[35]:

$$v_t = \frac{1}{18} d^2 \frac{(\rho_{Fe} - \rho_{Al_2O_3})}{\eta} g \qquad [3]$$

where v_t, d, ρ_i, η, and g are terminal velocity, particle diameter, density of the i phase, viscosity of molten steel, and gravitational acceleration, respectively. In the current study, the terminal velocity of alumina agglomerates was calculated by using the thermophysical properties listed in Table II. The terminal velocity was plotted against the inclusion size (Figure 6). Because the melt height was about 44 mm in the current experiments, an inclusion (aggregate) had to have a diameter of at least 9 μm to float from the bottom of the crucible up to the melt surface over a 30-minute period. As shown in Figure 6(b), inclusions with diameters ranging in size from 2 to 4 μm were plentiful, as were inclusions with diameters greater than 10 μm that formed through agglomeration. The latter would easily float up (Eq. [3]) and thus be removed from the melt after 30 min.

2. *Ce-Al deoxidation*

Because cerium is a stronger deoxidizer than aluminum, based on Eqs. [1] and [2], the driving force for the formation of Ce_2O_3 is greater than that for Al_2O_3. However, because the content of oxygen in equilibrium with 0.2 mass pct Al is comparable to that in equilibrium with mass pct Ce being from 0.03 to 0.1 (15- to 30-minute samples) from the computational results shown in Figure 7, both Ce_2O_3 and Al_2O_3 could be nucleated

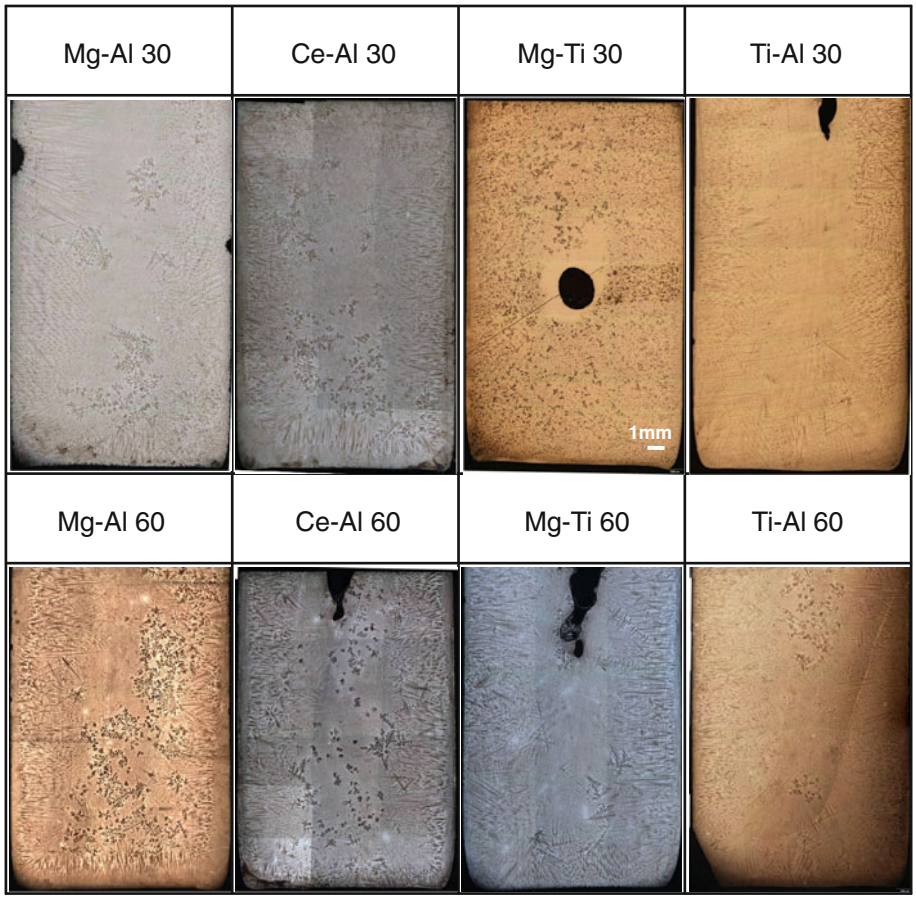

Fig. 4—Optical microscopy of the solidified structures of the deoxidized samples.

Table I. Chemical Compositions and Characteristics of Inclusions in the Various Samples

Deoxidizer Combination	Time (min)	Tot. [O] (mass ppm)	Type of Inclusions	Major Inclusion	Inclusion Density (ea mm^{-3})
Mg-Al	30	14	Al_2O_3, $MgAl_2O_4$	Al_2O_3	1.01×10^6
	60	11	$MgAl_2O_4$, Al_2O_3	$MgAl_2O_4$	2.20×10^5
Ce-Al	30	11	Ce_2O_3, Al_2O_3	Ce_2O_3	2.37×10^5
	60	26	Al_2O_3, Ce_2O_3	Al_2O_3	2.15×10^6
Mg-Ti	30	25	MgO($MgAl_2O_4$)-TiN, $MgAl_2O_4$, MgO, TiN,	MgO($MgAl_2O_4$)-TiN	4.13×10^5
	60	13	Ti_2O_3, TiN	Ti_2O_3	8.94×10^5
Ti-Al	30	9	Al_2O_3, TiN	Al_2O_3	6.42×10^5
	60	29	Al_2O_3, TiN	Al_2O_3	7.74×10^5

competitively. We computed the deoxidation equilibrium using FactSage™6.2, a commercial thermochemical software package.[36,37] We have confirmed the usefulness and reliability of this software in predicting deoxidation equilibria and related phase stability diagrams in previous studies.[29,34,38,39] However, because of the significantly low residual content of Ce (about 5 mass ppm) compared to that of Al in the 60-minute sample, the content of oxygen in the melt could not be determined by Ce; instead, we used Al, as shown in Figure 7(a). The evolution path of inclusions in samples to which the Ce-Al complex was added for deoxidation is shown in the Al-Ce-O stability diagram (Figure 7(b)), which was computed using FactSage™6.2. The first phase that formed was a Ce_2O_3-rich phase, followed by a Al-Ce-O (mainly $AlCeO_3$) complex oxide, and finally Al_2O_3-rich inclusions due to the decreased content of cerium.

These calculation results agree well with the SEM-based element mapping of inclusions, as shown in Figure 8. In the 30-minute sample, we found Al_2O_3-Ce_2O_3 compounds, whereas fine Al_2O_3-rich particles were present together with a small amount of Ce_2O_3 inclusions in the 60-minute sample.

3. *Mg-Ti Deoxidation*

When Mg-Ti was used for deoxidation, both MgO-Al_2O_3 compounds and TiN were detected as confirmed

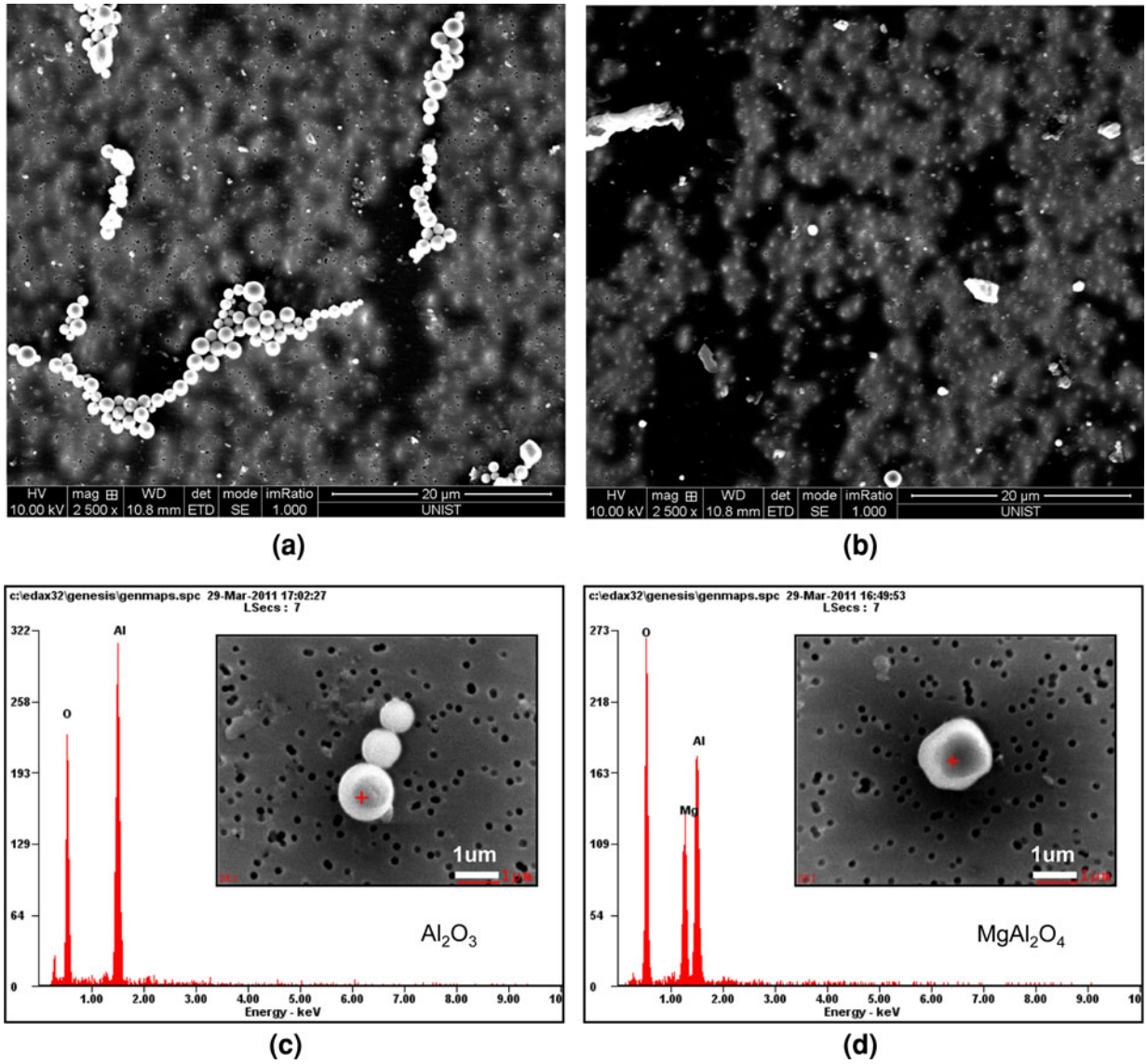

Fig. 5—SEM images showing typical inclusion morphology, *i.e.*, alumina at 30 min (*a*) and spinel at 60 min (*b*) and EDS data for alumina at 30 min (*c*) and spinel at 60 min (*d*) in the case of Mg-Al deoxidation.

from the SEM-EDS element mapping data, and as shown in Figure 9. Even though Mg-Ti was added to the alloy melt, the inclusions containing aluminum probably formed because of the dissolution of Al from the thermocouple sheath tube and/or the crucible. These complex inclusions had oxide at the core surrounded by nitride, as shown in Figure 10. However, because the nitrogen content in the alloy melt was very low in the current experiments, *i.e.*, less than 10 mass ppm (Figure 2(b)), the formation of TiN was not feasible with regard to the thermodynamics of homogeneous nucleation. Therefore, these results imply that the formation of TiN is energetically possible when appropriate oxides such as MgO and $MgAl_2O_4$ exist in the melt as heterogeneous nucleation substrates. Suito *et al.*[27,40] reported that if appropriate oxides are present in the melt, the product of Ti and N for the precipitation of TiN could be lower than the equilibrium value for homogeneous nucleation in the absence of these oxides.

Table II. Data Used to Calculate the Terminal Velocity of Al_2O_3

Symbol	Value[46]	Unit	Notation
g	9.8	m/s^2	gravitational acceleration
ρ_{Fe}	7.0	g/cm^3	density of molten Fe
$\rho_{alumina}$	3.97	g/cm^3	density of alumina
η	0.005	N s/m^2	viscosity of molten Fe
v_t		m/s	terminal velocity of alumina

They confirmed this in their study by demonstrating that almost all inclusions were MgO + TiN rather than single TiN and single MgO particles when they used Mg-Ti for deoxidation.[27,40]

The nucleation of TiN on MgO and/or $MgAl_2O_4$ can be understood by the lattice disregistry concept. The lattice disregistry, which was defined by Bramfitt as

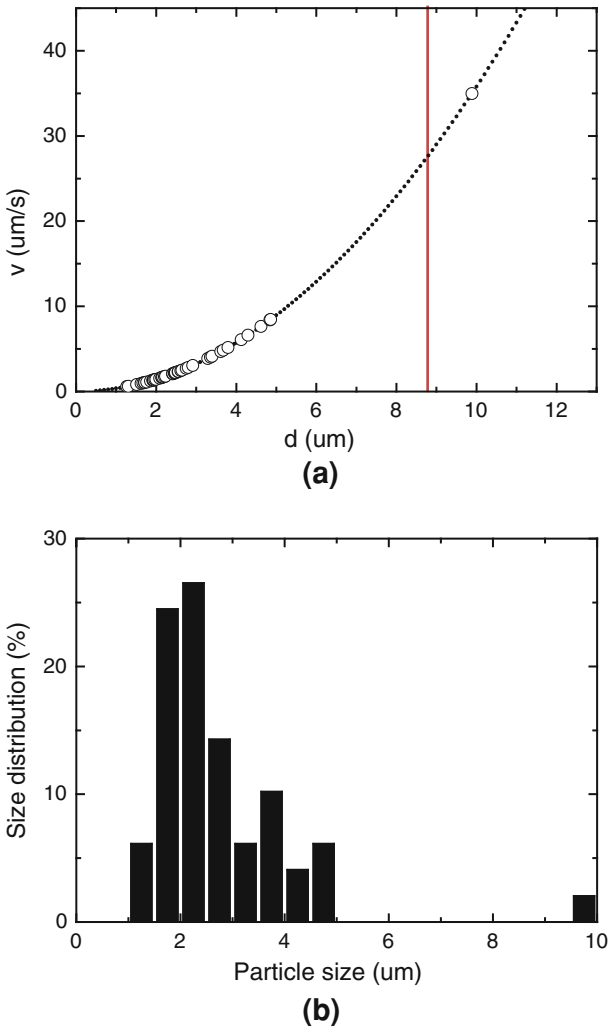

Fig. 6—Terminal velocity of agglomerate Al_2O_3 *vs* the diameter of inclusion (*a*) and the size distribution (*b*) for the Mg-Al 30-min sample.

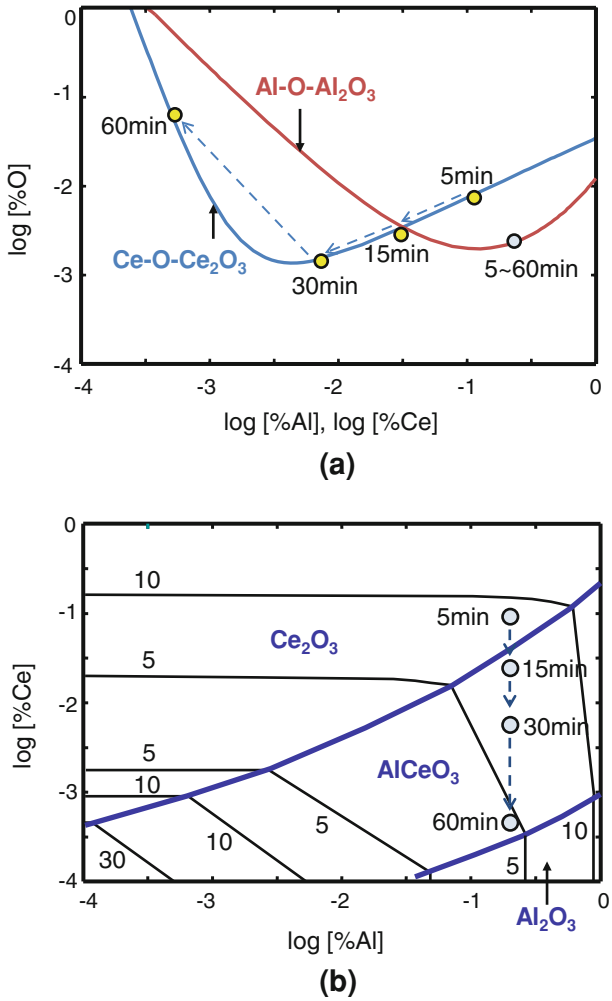

Fig. 7—Phase stability diagram of inclusions with iso-oxygen (mass ppm) contours in the Fe-2 mass pct Ni-1 mass pct Mn-1 mass pct Mo-Ce-Al alloy at 1873 K (1600 °C) as calculated using FactSage™6.2 software.

Eq. [4],[21] between MgO and TiN is about 0.05 pct, indicating a nearly epitaxial interface, while that between $MgAl_2O_4$ and TiN is about 4.9 pct, as listed in Table III.

$$\delta_{(hkl)_n}^{(hkl)_s} = \sum_{i=1}^{3} \left(\frac{\left| (d_{[uvw]_s^i} \cos\theta) - d_{[uvw]_n^i} \right|}{3 \times d_{[uvw]_n^i}} \right) \times 100 \qquad [4]$$

where $(hkl)_s$, a low-index plane of the substrate; $[uvw]_s$, a low-index direction in $(hkl)_s$; $(hkl)_n$, a low-index plane in the nucleated solid; $[uvw]_n$, a low-index direction in $(hkl)_n$; $d_{[uvw]_n}$, the distance between a nonmetallic element along $[uvw]_n$ (if the compound has a single element, $d_{[uvw]_n}$ is the interatomic spacing along $[uvw]_n$); $d_{[uvw]_s}$, the distance between the nonmetallic element along $[uvw]_s$ (if the compound has a single element; $d_{[uvw]_s}$ is the interatomic spacing along $[uvw]_s$), and θ, the angle between the $[uvw]_s$ and $[uvw]_n$.

Consequently, the lattice disregistry between δ-iron and $MgAl_2O_4$, MgO, and TiN is about 1.2, 4.0 and 3.9 pct, respectively. This means that these oxide and nitride particles have a high potential for promoting the heterogeneous nucleation of δ-iron during the solidification process. This is in good agreement with the solidification structures shown in Figure 4. In fact, in a previous study, we confirmed the effectiveness of $MgAl_2O_4$, which was not combined with TiN, on the nucleation of δ-iron during rapid solidification of Fe-2 mass pct Ni-1 mass pct Mo-1 mass pct Mn alloy melts.[41]

In contrast, in the 60-minute samples, inclusions containing Mg and Al were not observed, as shown in Figure 9(b). Because magnesium is very active, the Mg content in the alloy melt decreased significantly to about 2 mass ppm (Figure 3(c)). Therefore, TiN and Ti_2O_3 compounds remained rather than Mg-base oxide inclusions—not only fine TiN particles, but also some Ti_2O_3 remained, as shown in Figure 11. Consequently, the poor equiaxed structure observed in the Mg-Ti-deoxidized 60-minute sample (Figure 4) could have been due to the very high lattice disregistry between Ti_2O_3 and δ-iron (about 26 pct), as shown in Table III. Notwithstanding the existence of TiN, the solidification structure

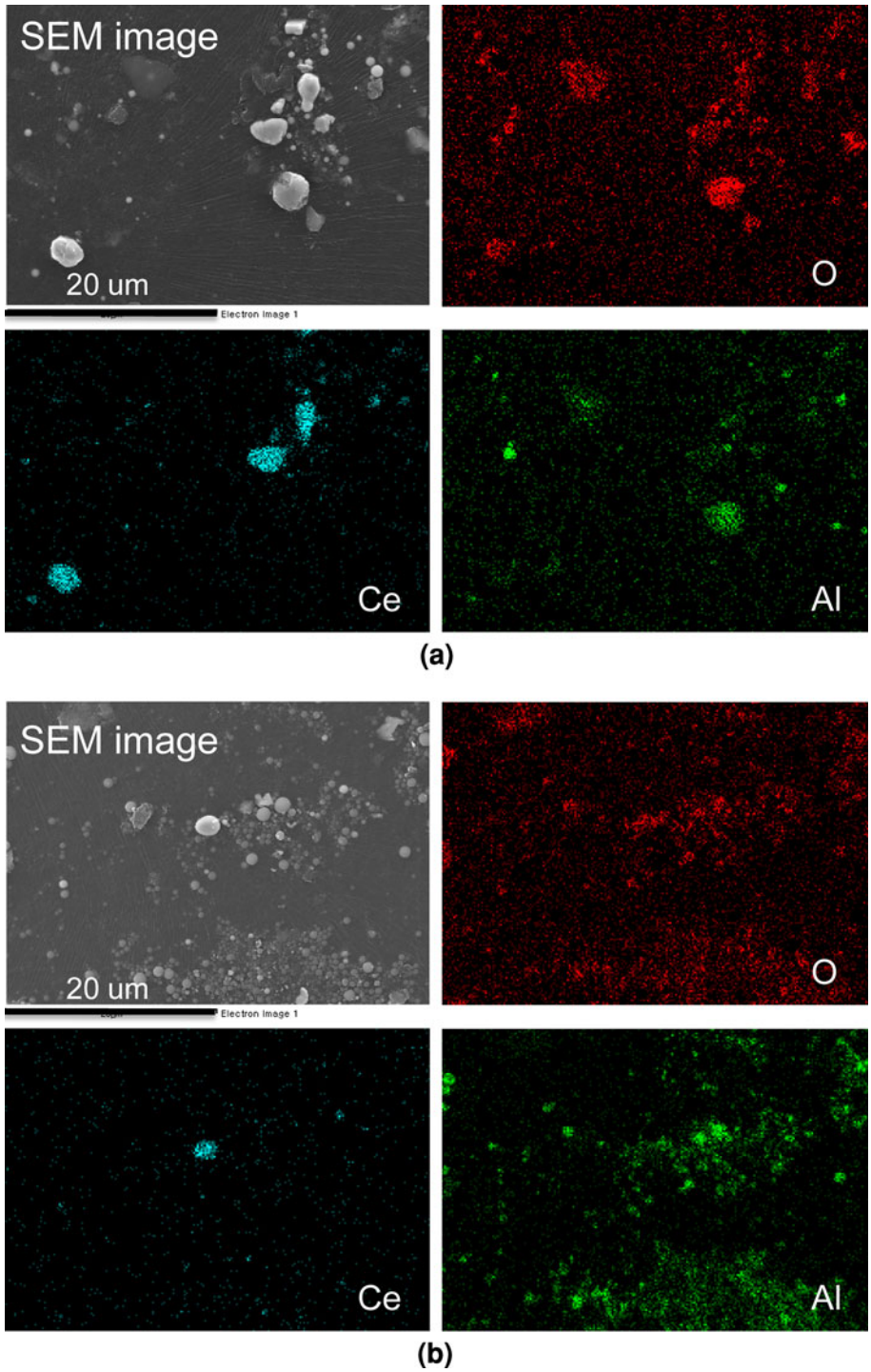

Fig. 8—SEM images showing the typical inclusion morphology and element mapping results for the 30-min (*a*) and 60-min (*b*) Ce-Al complex deoxidation samples.

was mainly columnar, indicating that the TiN in this sample was not effective. This is probably because the TiN observed in the 60-minute sample could have been formed during solidification by solute enrichment in the interdendritic region because of the relatively low equilibrium solid/liquid partitioning coefficient of Ti, *i.e.*, $k_{Ti} = 0.36$.[30]

Thus, the tiny TiN particles that formed through microsegregation during cooling were not able to act as heterogeneous nucleation sites.[29] This result agrees well with the previous findings that formation of an equiaxed grain occurs if the formation temperature of TiN is higher than the liquidus temperature of the steel.[29,42,43]

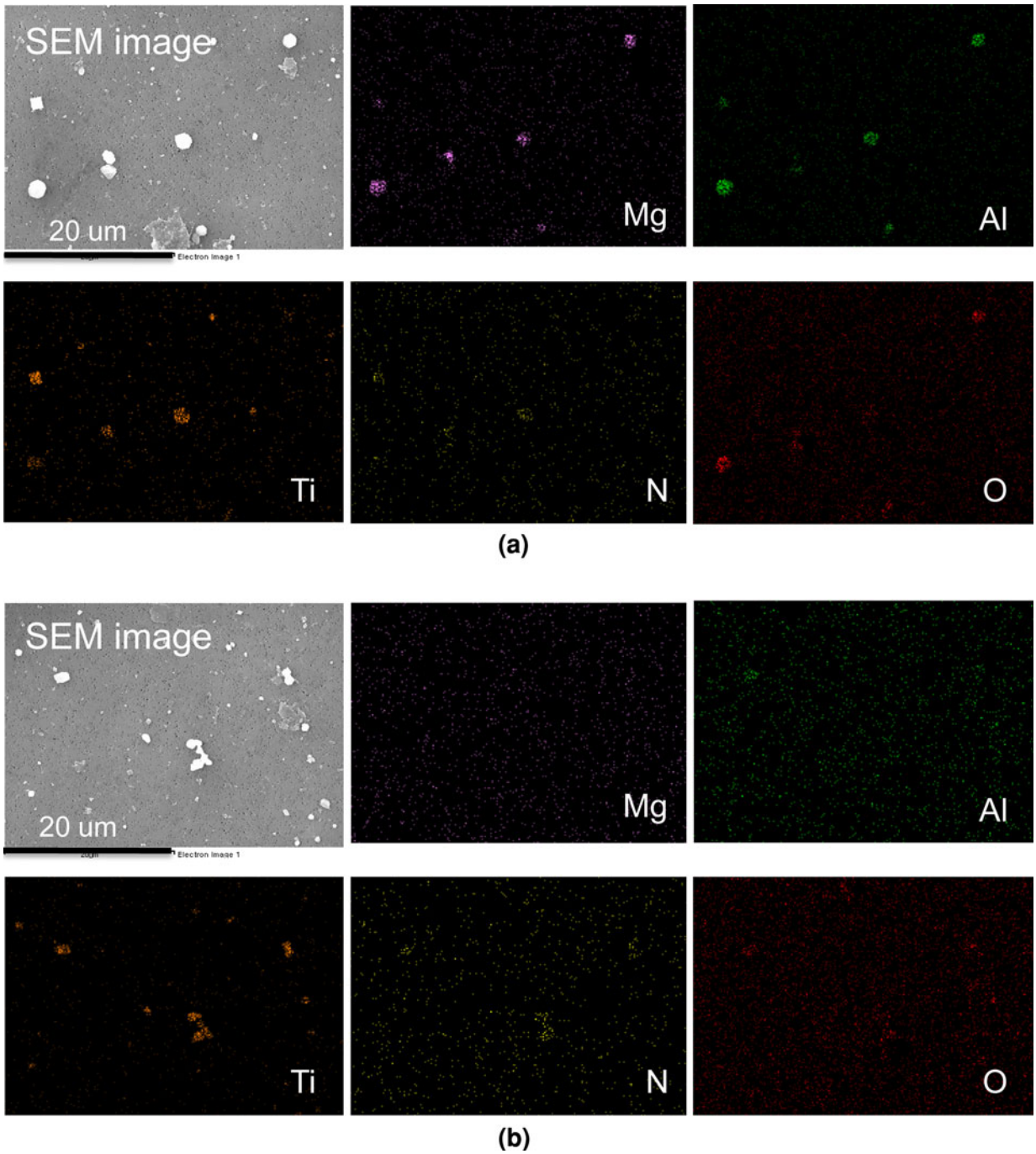

Fig. 9—SEM images showing the typical inclusion morphology and element mapping results for the 30-min (*a*) and 60-min (*b*) Mg-Ti complex deoxidation samples.

4. *Ti-Al deoxidation*

In the Ti-Al experiment, the inclusion number density and chemistry remained stable throughout the experiment. The inclusions formed were mainly alumina and very fine TiN, as shown in Figure 12. The alumina was the major inclusion because of its thermodynamic stability, as shown in the thermodynamic stability diagram in Figure 13, while very fine TiN precipitated during cooling, as discussed in the previous section.

B. *Effect of Non-Metallic Inclusions on the Solidification Structure*

The number density of inclusions in the current samples varied from 10^5 to 10^6/ mm^3, as shown in Table I. Furthermore, the chemistry of inclusions and thus the dominant compound changed with reaction time with the exception of the Ti-Al deoxidation experiment. We will discuss the fine equiaxed grain structure obtained in the 30-minute Mg-Ti-deoxidized

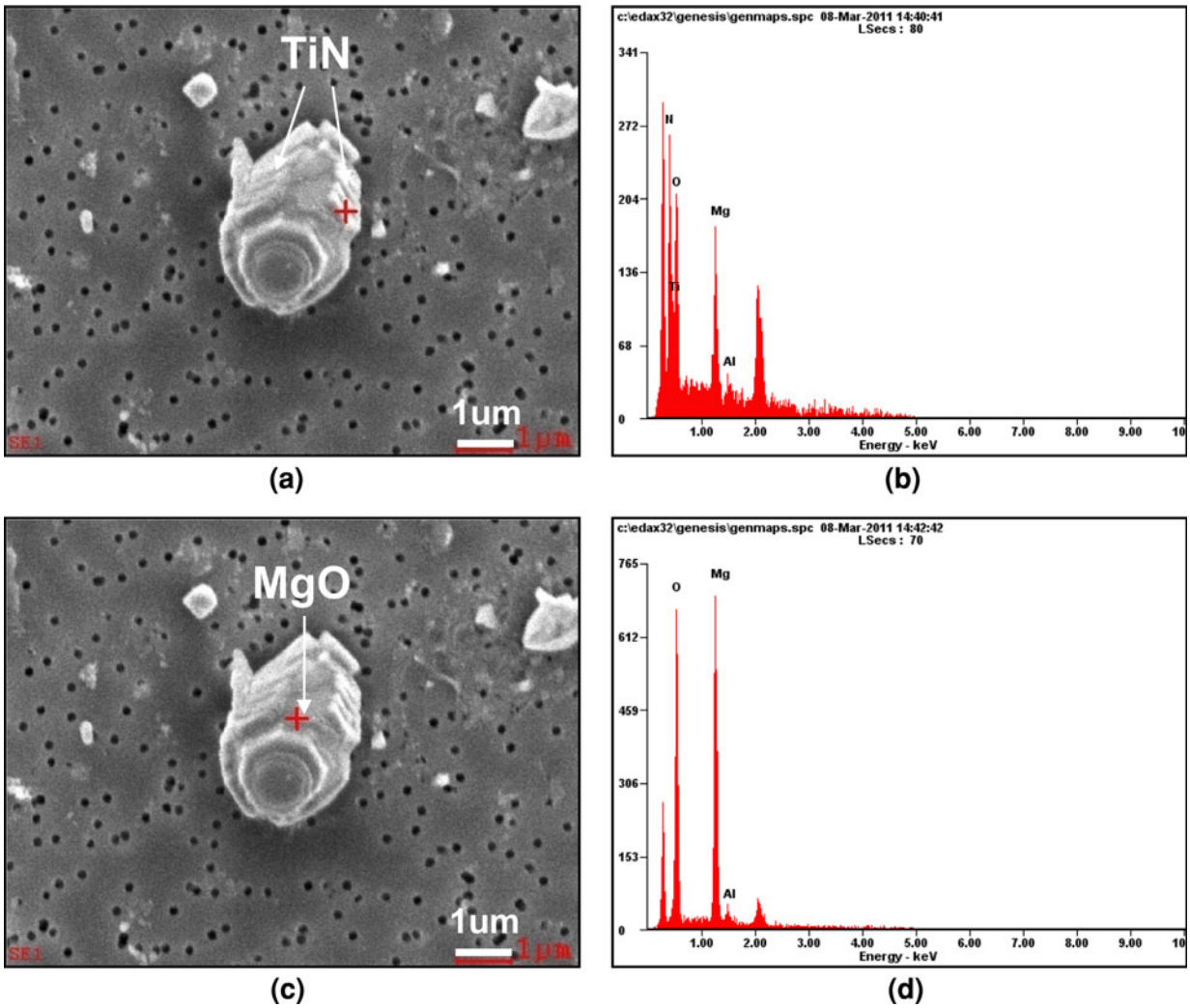

Fig. 10—SEM images showing the complex inclusions (*a*), (*c*) and EDS data for the complex inclusions in the surrounding (*b*) and core (*d*) of the 30-min Mg-Ti sample.

Table III. Disregistry Data for Delta Fe and TiN with Various Inclusions

Inclusion	Disregistry with Delta Fe (pct)	Disregistry with TiN (pct)	Lattice Parameter (α) (At 1811 K [1538 °C)]
Al_2O_3	10.41	17.48	a = 4.825[47]
Ce_2O_3	5.01	29.28	a = 3.938[22]
MgO	3.97	0.053	a = 4.310[47]
Ti_2O_3	18.90	16.17	a = 5.225[23]
$MgAl_2O_4$	1.16	4.88	a = 8.195[47]
TiN	3.91	–	a = 4.308[21]

sample and the fully columnar structure of the 30-minute Ti-Al-deoxidized 30-minute sample in more detail.

Although alumina inclusions were present in the melt, there were no equiaxed crystals in the Ti-Al 30-minute sample, indicating that alumina cannot act as an effective inoculant for heterogeneous nucleation of δ-iron. A similar tendency was observed in the Mg-Al 30-minute sample, which had relatively poor equiaxed crystals.

In contrast, a number of heterogeneous nucleation catalysts were present in the Mg-Al 60-minute sample. However, few studies have investigated the effect of $MgAl_2O_4$ on grain refinement. Fujimura *et al.*[44] concluded that $MgAl_2O_4$ helps heterogeneous nucleation of TiN because of low disregistry between these two substances (4.9 pct), resulting in the formation of an equiaxed grain structure. However, $MgAl_2O_4$ spinel itself did not promote the nucleation of δ-iron despite the very low disregistry between $MgAl_2O_4$ and δ-iron

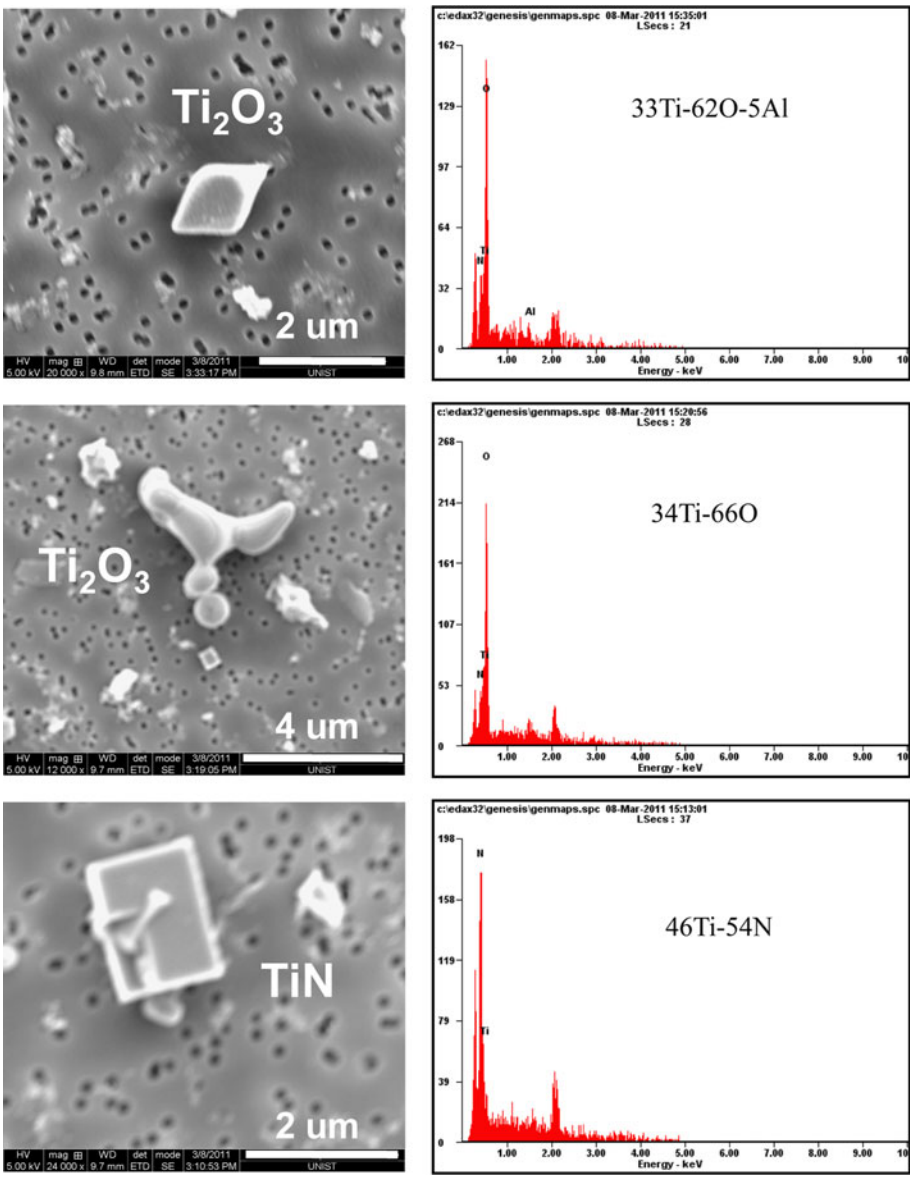

Fig. 11—SEM images and EDS data of typical inclusions in the Mg-Ti 60-min sample. The numbers indicate the atomic pct of each element.

(1.2 pct). It is not clear why this should be so. Isobe reported that Mg deoxidation facilitated the formation of an equiaxed zone of low carbon steel because of the formation of MgO and/or $MgAl_2O_4$, and that this effect was more significant in Ti-containing steel because of the formation of MgO-TiN complex compounds.[45] More recently, we reported that Mg deoxidation also enhanced the formation of equiaxed crystals in the Fe-2 mass pct Ni-1 mass pct Mn-1 mass pct Mo alloy through the formation of MgO and $MgAl_2O_4$ because of low disregistry with the δ-iron, *i.e.*, about 4.0 pct and 1.2 pct (Table III), respectively.[41]

In summary, Ce_2O_3 and $MgAl_2O_4$ as well as MgO($MgAl_2O_4$)-TiN complex compounds are good catalysts for nucleation of δ-iron, whereas Al_2O_3 and Ti_2O_3 do not contribute to the formation of equiaxed crystals. The MgO($MgAl_2O_4$)-TiN complex compounds are the most effective. Consequently, for grain refinement of a rapidly solidified structure, complex deoxidation using Mg-Ti and Mg-Al is preferable to that using Ti-Al and Ce-Al. Furthermore, lattice disregistry, even though it is not the only factor that affects grain refinement, can be exploited to control the heterogeneous nucleation tendency.

V. CONCLUSIONS

The effect of combinations of several deoxidizers, *i.e.*, Mg-Al, Mg-Ti, Al-Ti, and Ce-Al, on the solidification structure of iron alloy melts was investigated using a melt sampling and quenching methodology. By employing this method, we were able to evaluate the catalytic potency of several complex inclusion particles by taking

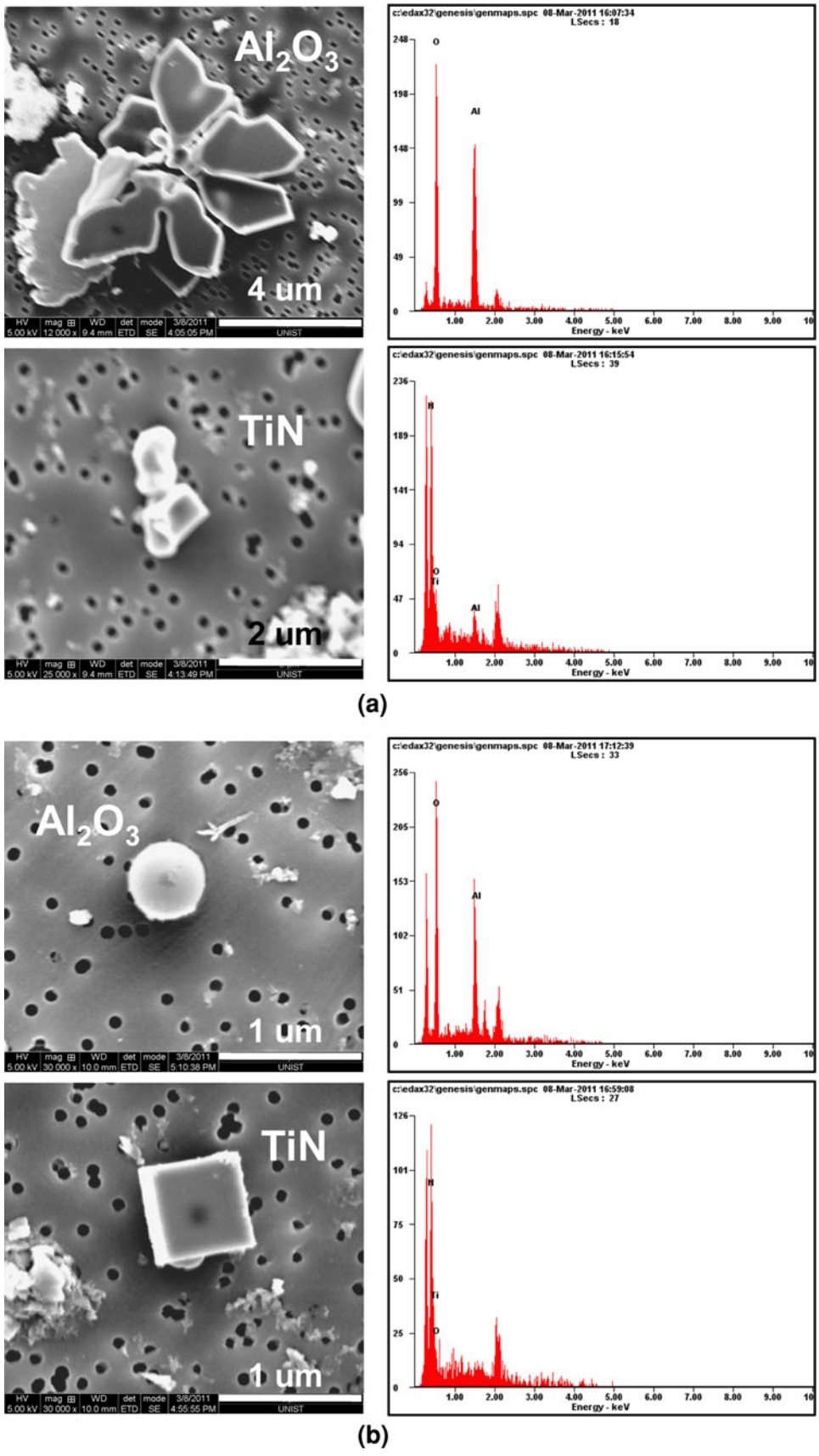

Fig. 12—SEM images and EDS data of typical inclusions in the 30-min Ti-Al sample (*a*), and 60-min Ti-Al sample (*b*).

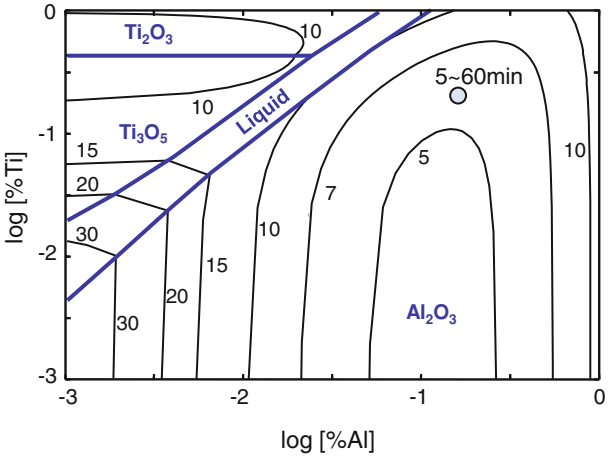

Fig. 13—Phase stability diagram of inclusions with iso-oxygen (mass ppm) contours in the Fe-2 mass pct Ni-1 mass pct Mn-1 mass pct Mo-Ti-Al alloy at 1873 K (1600 °C) as calculated using FactSage™6.2 software.

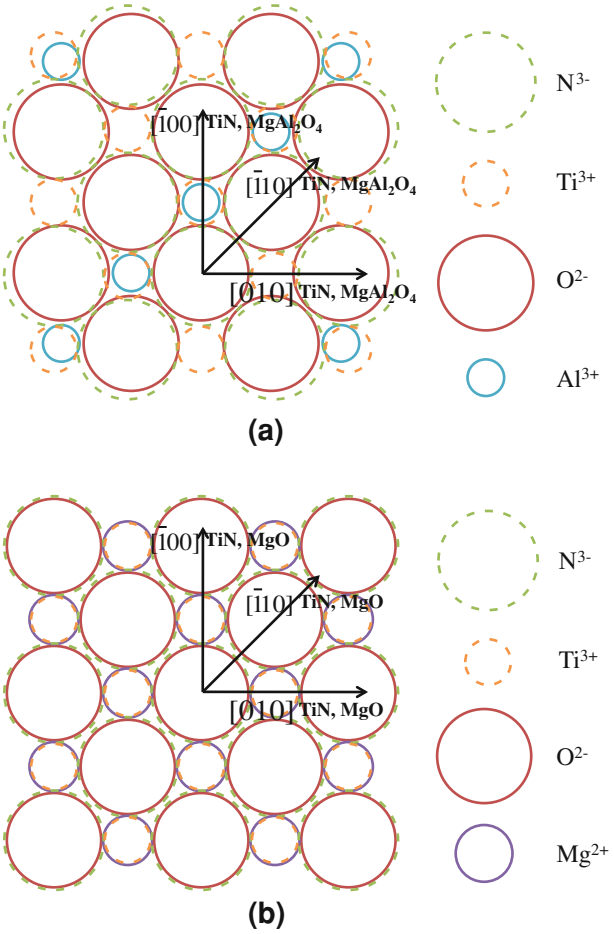

Fig. A1—The crystallographic relationship at the interface between (100)TiN and (100)$MgAl_2O_4$ (*a*), and between (100)TiN and (100)MgO (*b*).

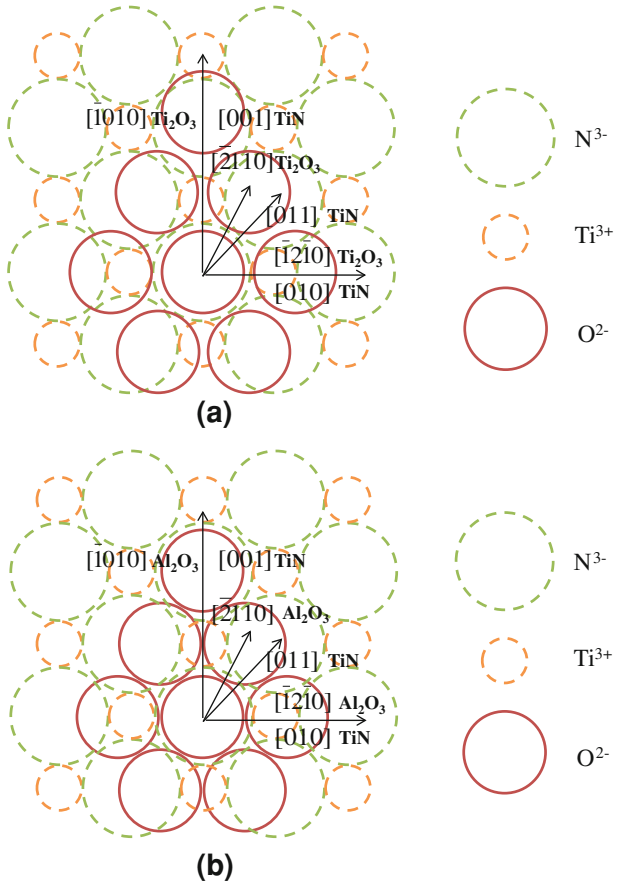

Fig. A2—The crystallographic relationship at the interface between (100)TiN and (0001)Ti_2O_3 (*a*), and between (100)TiN and (0001)Al_2O_3 (*b*).

the inclusion evolution process into account. Our major findings were as follows:

1. Fine equiaxed crystals were obtained in Mg-Ti-deoxidized steel wherein MgO($MgAl_2O_4$)-TiN complex compounds formed. However, the longer the holding time at high temperatures, the larger the fraction of Ti_2O_3, and very fine TiN formed because of microsegregation during solidification, resulting in poor equiaxed crystals.
2. When the steel was deoxidized using Mg-Al, the initial structure was dominantly columnar. However, as the holding time at a high temperature increased, so did the fraction of $MgAl_2O_4$ spinel, resulting in the formation of fine equiaxed crystals.
3. Ce-Al complex deoxidation resulted in a relatively small portion of equiaxed crystals, whereas Ti-Al deoxidation was the least effective in terms of the formation of equiaxed crystals because of the formation of alumina.
4. The effectiveness of each inoculant particle for the crystallization of primary δ-iron was explained well by the lattice disregistry as calculated by Bramfitt's relation.

APPENDIX

To illustrate the calculation of disregistry, we provide examples for several oxide inclusions nucleating TiN.[21] In these examples, the $MgAl_2O_4$ spinel, Al_2O_3, MgO, and Ti_2O_3 were selected as nucleation sites for TiN. The crystallographic relationships of each case are illustrated in Figures A1 and A2, and the corresponding parameters for Eq. [4] are listed in Table IV.

Case I; $MgAl_2O_4(100)//TiN(100)$

As shown in Figure A1(a), the (100) plane of TiN is superimposed on the (100) plane of spinel. The three lowest-index directions of TiN and $MgAl_2O_4$ are $[\bar{1}00]$, $[\bar{1}10]$ and [010]. The distances along these directions are given in Table IV. In accordance with Eq. [4], the disregistry equation for Case 1 was written as follows:

$$\delta^{(100)_{MgAl_2O_4}}_{(100)_{TiN}} = \frac{1}{3}\left(\frac{\left|(d_{[\bar{1}00]_{MgAl_2O_4}}\cos\theta) - d_{[\bar{1}00]_{TiN}}\right|}{d_{[\bar{1}00]_{TiN}}} + \frac{\left|(d_{[\bar{1}10]_{MgAl_2O_4}}\cos\theta) - d_{[\bar{1}10]_{TiN}}\right|}{d_{[\bar{1}10]_{TiN}}} + \frac{\left|(d_{[010]_{MgAl_2O_4}}\cos\theta) - d_{[010]_{TiN}}\right|}{d_{[010]_{TiN}}}\right) \times 100$$

$$= \frac{1}{3}\left(\frac{|4.098 - 4.308|}{4.308} + \frac{|2.897 - 3.046|}{3.046} + \frac{|4.098 - 4.308|}{4.308}\right) \times 100 = 4.88\,\text{pct}$$

Case II; $MgO(100)//TiN(100)$

As shown in Figure A1(b), the (100) plane of TiN is superimposed on the (100) plane of MgO. Using a similar analysis to that used in Case I, Eq. [4] was written as follows:

$$\delta^{(100)_{MgO}}_{(100)_{TiN}} = \frac{1}{3}\left(\frac{\left|(d_{[\bar{1}00]_{MgO}}\cos\theta) - d_{[\bar{1}00]_{TiN}}\right|}{d_{[\bar{1}00]_{TiN}}} + \frac{\left|(d_{[\bar{1}10]_{MgO}}\cos\theta) - d_{[\bar{1}10]_{TiN}}\right|}{d_{[\bar{1}10]_{TiN}}} + \frac{\left|(d_{[010]_{MgO}}\cos\theta) - d_{[010]_{TiN}}\right|}{d_{[010]_{TiN}}}\right) \times 100$$

$$= \frac{1}{3}\left(\frac{|4.310 - 4.308|}{4.308} + \frac{|3.048 - 3.046|}{3.046} + \frac{|4.310 - 4.308|}{4.308}\right) \times 100 = 0.053\,\text{pct}$$

Case III; $Ti_2O_3(0001)//TiN(100)$

Because the lattice disregistry is 23.46 pct for the (110) plane of TiN and 48.36 pct for the (111) plane of TiN, the (100) of TiN is superimposed on the (0001) plane of Ti_2O_3, as shown in Figure A2(a). Equation [4] was therefore written as:

$$\delta^{(0001)_{Ti_2O_3}}_{(100)_{TiN}} = \frac{1}{3}\left(\frac{\left|(d_{[\bar{1}2\bar{1}0]_{Ti_2O_3}}\cos\theta) - d_{[010]_{TiN}}\right|}{d_{[001]_{TiN}}} + \frac{\left|(d_{[\bar{2}110]_{Ti_2O_3}}\cos\theta) - d_{[011]_{TiN}}\right|}{d_{[1\bar{1}1]_{TiN}}} + \frac{\left|(d_{[\bar{1}010]_{Ti_2O_3}}\cos\theta) - d_{[001]_{TiN}}\right|}{d_{[1\bar{1}0]_{TiN}}}\right) \times 100$$

$$= \frac{1}{3}\left(\frac{|3.146 - 4.308|}{4.308} + \frac{|3.039 - 3.046|}{3.046} + \frac{|5.225 - 4.308|}{4.308}\right) \times 100 = 16.17\,\text{pct}$$

Table IV. Parameters Used for the Disregistry Calculations

Case	$[uvw]_s$	$[uvw]_n$	$d[uvw]_s$	$d[uvw]_n$	θ (deg)	$d[uvw]_s$ (cos θ)
(100)$MgAl_2O_4$||(100)TiN	$[\bar{1}00]MgAl_2O_4$	$[\bar{1}00]$TiN	4.098	4.308	0	4.098
	$[\bar{1}10]MgAl_2O_4$	$[\bar{1}10]$TiN	2.897	3.046	0	2.897
	$[010]MgAl_2O_4$	[010]TiN	4.098	4.308	0	4.098
(100)MgO||(100)TiN	$[\bar{1}00]$MgO	$[\bar{1}00]$TiN	4.310	4.308	0	4.310
	$[\bar{1}10]$MgO	$[\bar{1}10]$TiN	3.048	3.046	0	3.048
	[010]MgO	[010]TiN	4.310	4.308	0	4.310
(0001)Ti_2O_3||(100)TiN	$[\bar{1}2\bar{1}0]Ti_2O_3$	[010]TiN	3.146	4.308	0	3.146
	$[\bar{2}110]Ti_2O_3$	[011]TiN	3.146	3.046	15	3.039
	$[\bar{1}010]Ti_2O_3$	[001]TiN	5.225	4.308	0	5.225
(0001)Al_2O_3||(100)TiN	$[\bar{1}2\bar{1}0]Al_2O_3$	[010]TiN	2.905	4.308	0	2.905
	$[\bar{2}110]Al_2O_3$	[011]TiN	2.905	3.046	15	2.806
	$[\bar{1}010]Al_2O_3$	[001]TiN	4.825	4.308	0	4.825

Case IV; $Al_2O_3(0001)//TiN(100)$

Because the lattice disregistry of the (110) plane of TiN is 23.7 pct and that of the (111) plane of TiN is 51.7 pct, the (100) plane of TiN is superimposed on the (0001) of Al_2O_3, as shown in Figure A2(b). Using a similar analysis as in Case III yielded the following Eq. [4]:

$$\delta^{(0001)_{Al_2O_3}}_{(100)_{TiN}} = \frac{1}{3}\left(\frac{\left|(d_{[\bar{1}2\bar{1}0]_{Al_2O_3}}\cos\theta) - d_{[010]_{TiN}}\right|}{d_{[010]_{TiN}}} + \frac{\left|(d_{[\bar{2}110]_{Al_2O_3}}\cos\theta) - d_{[011]_{TiN}}\right|}{d_{[011]_{TiN}}} + \frac{\left|(d_{[\bar{1}010]_{Al_2O_3}}\cos\theta) - d_{[001]_{TiN}}\right|}{d_{[001]_{TiN}}}\right) \times 100$$

$$= \frac{1}{3}\left(\frac{|2.905 - 4.308|}{4.308} + \frac{|2.806 - 3.046|}{3.046} + \frac{|4.825 - 4.308|}{4.308}\right) \times 100 = 17.48\,\text{pct}$$

REFERENCES

1. Ø. Grong: *Metallurgical Modeling of Welding*, 2nd ed., Institute of Materials, London, 1997, pp. 221–300.
2. Ø. Grong and D.K. Matlock: *Int. Met. Rev.*, 1986, vol. 31, pp. 27–48.
3. O.M. Akselsen, Ø. Grong, and P.E. Kvaale: *Metall. Mater. Trans. A*, 1986, vol. 17A, pp. 1529–36.
4. J. Takamura and S. Mizuguchi: *Proceedings of the Sixth International Iron and Steel Congress*, 3rd ed., ISIJ, Tokyo, 1990, pp. 591–97.
5. E.A. Metzbower, H.K.D.H. Bhadeshia, and R.H. Phillips: *Mater. Sci. Technol.*, 1994, vol. 10, pp. 56–59.
6. Z. Yang and T. Debroy: *Metall. Mater. Trans. B*, 1999, vol. 30B, pp. 483–93.
7. T. Koseki and G. Thewlis: *Mater. Sci. Technol.*, 2005, vol. 21, pp. 867–79.
8. G. Thewlis: *Mater. Sci. Technol.*, 2006, vol. 22, pp. 153–66.
9. K.S. Bang, C. Park, and S. Liu: *J. Mater. Sci.*, 2006, vol. 41, pp. 5994–6000.
10. T. Koseki, H. Kato, M. Tsutsumi, K. Kasaki, and J. Inoue: *Int. J. Mater. Res.*, 2008, vol. 99, pp. 347–51.
11. H.K. Sung, S.Y. Shin, W. Cha, K. Oh, S. Lee, and N.J. Kim: *Mater. Sci. Eng. A*, 2011, vol. 528, pp. 3350–57.
12. H. Suito, A.V. Karasev, M. Hamada, R. Inoue, and K. Nakajima: *ISIJ Int.*, 2011, vol. 51, pp. 1151–62.
13. J.L. Caron, S.S. Babu, and J.C. Lippold: *Metall. Mater. Trans. A*, 2011, vol. 42A, pp. 4015–31.
14. A.O. Kluken, Ø. Grong, and G. Rørvik: *Metall. Trans. A*, 1990, vol. 21A, pp. 2047–58.
15. H. Terasaki and Y. Komizo: *Sci. Technol. Weld. Join.*, 2006, vol. 11, pp. 561–66.
16. T. Yamada, H. Terasaki, and Y. Komizo: *Sci. Technol. Weld. Join.*, 2008, vol. 13, pp. 118–25.
17. T. Koseki, S. Ohkita, and N. Yurioka: *Sci. Technol. Weld. Join.*, 1997, vol. 2, pp. 65–9.
18. Y. Ito and M. Nakanishi: *Sumitomo Search*, 1976, vol. 15, pp. 42–62.
19. N. Mori, H.Homma, M. Wakabayshi, and S. Ohkita: *J. Jpn. Weld. Soc.*, 1981, vol. 50, pp. 786–93.
20. T. Nishizawa: *ISIJ Int.*, 2000, vol. 40, pp. 1269–74.
21. B.L. Bramfitt: *Metall. Trans.*, 1970, vol. 1, pp. 1987–95.
22. T. Ohashi, T. Hiromoto, H. Fujii, Y. Nuri, and K. Asano: *Tetsu-to-Hagané*, 1976, vol. 62, pp. 614–23.
23. K. Nakajima, H. Hasegawa, S. Khumkoa, and S. Mizoguchi: *Metall. Mater. Trans. B*, 2003, vol. 34B, pp. 539–47.
24. K. Nakajima, H. Ohta, H. Suito, and P. Jönsson: *ISIJ Int.*, 2006, vol. 46, pp. 807–13.
25. K. Sakata and H. Suito: *Metall. Mater. Trans. B*, 1999, vol. 30B, pp. 1053–63.
26. M. Guo and H. Suito: *ISIJ Int.*, 1999, vol. 39B, pp. 722–29.
27. G.V. Pervushin and H. Suito: *ISIJ Int.*, 2001, vol. 41, pp. 728–37.
28. H. Ohta and H. Suito: *ISIJ Int.*, 2006, vol. 46, pp. 22–28.
29. J.H. Park: *CALPHAD*, 2011, vol. 35, pp. 455–62.
30. T. Koseki, H. Inoue, Y. Fukuda, and A. Nogami: *Sci. Technol. Adv. Mater.*, 2003, vol. 4, pp. 183–95.
31. S. Mridha and D.H. Jack: *Metallography*, 1982, vol. 15, pp. 163–75.
32. J.H. Park, D.J. Kim, and D.J. Min: *Metall. Mater. Trans. A*, 2012, vol. 43A, pp. 2316–24.
33. M. Hino and K. Ito: *Thermodynamic Data for Steelmaking*, Tohoku University Press, Sendai, 2010, pp. 10–34.
34. J.H. Park and H. Todoroki: *ISIJ Int.*, 2010, vol. 50, pp. 1333–46.
35. D.R. Poirier and G.H. Geiger: *Transport Phenomena in Materials Processing*, TMS, Warrendale, PA, 1994, pp. 62–71.
36. www.factsage.com (accessed October 2011).
37. C.W. Bale, E. Belisle, P. Chartrand, S.A. Decterov, G. Eriksson, K. Hack, I.H. Jung, Y.B. Kang, J. Melancon, A.D. Pelton C. Robelin, and S. Petersen: *CALPHAD*, 2009, vol. 33, pp. 295–311.
38. J.H. Park and Y.B. Kang: *Metall. Mater. Trans. B*, 2006, vol. 37B, pp. 791–98.
39. J.H. Park, S.B. Lee, and H.R. Gaye: *Metall. Mater. Trans. B*, 2008, vol. 39, pp. 853–61.
40. G.V. Pervushin and H. Suito: *ISIJ Int.*, 2001, vol. 41, pp. 748–56.
41. J.H. Park, J.S. Park, Y. Huh, and C.H. Lee: unpublished research.
42. T. Koseki and H. Inoue: *J. Jpn Inst. Met.*, 2001, vol. 65, pp. 644–51.
43. T. Koseki: *Bull. Iron Steel Inst. Jpn.*, 2010, vol. 15, pp. 30–35.
44. H. Fujimura, S. Tsuge, Y. Komizo, and T. Nishizawa: *Tetsu-to-Hagané*, 2001, vol. 87, pp. 29–34.
45. K. Isobe: *ISIJ Int.*, 2010, vol. 50, pp. 1972–80.
46. M. Wako and N. Sano: *ISIJ Int.*, 2007, vol. 47, pp. 627–32.
47. G. Fiquet, P. Richet, and G. Montagnac: *Phys. Chem. Miner.*, 1999, vol. 27, pp. 103–11.